Measurement 218 (2023) 113212

Contents lists available at ScienceDirect

Measurement

journal homepage: www.elsevier.com/locate/measurement

Double active thermographic inspection of additive manufacturing composites: numerical modelling and validation

Henrique V. Silva [a], Ana P. Martins [a], Miguel A. Machado [a,b], Telmo G. Santos [a,b], Marta S. Carvalho [a,b,*]

[a] UNIDEMI, Department of Mechanical and Industrial Engineering, NOVA School of Science and Technology, Universidade NOVA de Lisboa, 2829-516 Caparica, Portugal
[b] Laboratório Associado de Sistemas Inteligentes, LASI, 4800-058 Guimarães, Portugal

ARTICLE INFO

Keywords:
Computational modelling
Double Active Transient Thermography (DATT)
Non-destructive testing (NDT)
Polymer-matrix composites (PMC)
Thermal analysis

ABSTRACT

This study investigates the Non-Destructive Testing (NDT) inspection of 3D-printed fibre-reinforced polymers, comparing the conventional Active Transient Thermography (ATT) technique with a novel variant known as Double Active Transient Thermography (DATT). Finite element models for the simulation of both inspection techniques are validated by evaluating two statistical measures to correlate the numerical results with the experimental responses. The thermal contrast obtained with DATT was approximately twice the one obtained with ATT, for all tested samples. Numerical models allowed an insight evaluation of the heat dissipation along the thickness of the specimens, specifically around the fibres and the defects. These validated numerical models evidenced a relevant tool to predict the results of thermal contrast and to optimize the inspection parameters.

1. Introduction

Thermography has recently seen significant advancements, making it a valuable addition to the Non-Destructive Testing (NDT) technique. Its key benefits include non-contact and non-intrusive inspection, the ability to produce images that can be overlaid with the part for easy results interpretation, the ability to quickly inspect large areas, and its suitability for automation. Additionally, results can often be obtained quickly, sometimes in real-time [1,2]. These advantages have led to its widespread use in a variety of fields such as medicine [3], engineering [4,5], physics [6], and cultural heritage [7].

The use of NDT for the inspection of parts produced by Additive Manufacturing (AM) is a challenging task; the most frequently used materials in AM are polymers, which have low thermal and electrical conductivity, and high attenuation of acoustic waves. Whereas other methods have shown limitations in detecting defects in these types of components, Active Transient Thermography (ATT) has proven effective [8].

In ATT, thermal contrast is, in most cases, obtained by delivering energy to the material, i.e., by heating it. However, this approach may not always be possible and safe for inspected materials such as biological materials and medical applications, or nuclear waste reservoirs, as studied by Lei *et al.* [9]. For those cases, Szymanik *et al.* [10] proposed the removal of energy from the system by cooling it to obtain a temperature gradient. Alternatively, Double Active Transient Thermography (DATT), recently proposed by Machado *et al.* [11] concerns a variant of the conventional ATT, in which both hot and cold thermal excitations are applied on opposite sides of the component to be inspected, with the aim of anticipating and increasing the thermal contrast in defect and non-defect zones. Several experiments were conducted, varying the instants at which the heat fluxes start, their duration, and intensity, as well as cooling methods. This high cold flow was achieved by means of pouring a coolant fluid into the sample, which makes it unattractive for its industrial implementation. Cooled air is an affordable and practical alternative that facilitates the use of this technique in different components and environments, and its industrial implementation is reasonable. Piero *et al.* [12] developed a low-cost, real-time automatic heating and cooling system for thermographic inspection of structures, being the forced cooling of the automatic inspection system composed of a vortex tube. This system is more suitable for industrial application, and therefore will be used during the experimental procedures conducted in the present study.

Nevertheless, it is crucial to improve inspection reliability by selecting adequate inspection parameters, in order to reduce inspection time and increase the thermal contrast. This requires considerable effort in the experimental setups and a large number of experiments to reach

* Corresponding author.

https://doi.org/10.1016/j.measurement.2023.113212
Received 23 January 2023; Received in revised form 12 May 2023; Accepted 10 June 2023
Available online 15 June 2023

Table 1
Main 3D printing characteristics.

Printing Speed [mm/s]	Printing Temperature [°C]	Printing Platform Temperature [°C]	Layer Thickness [mm]	Line Width [mm]	Fan Speed	
					1st Layer	Remaining Layers
[1–6]	200	60	0.8	1.3	0%	100%

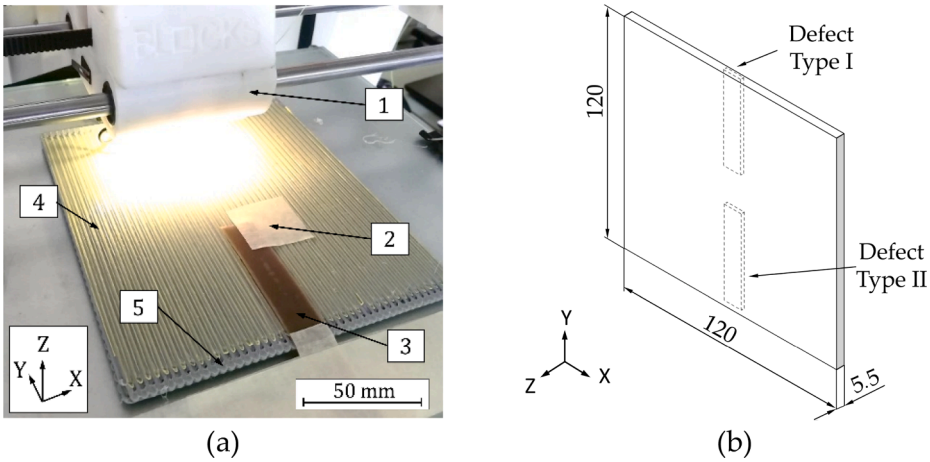

Fig. 1. Representation of the (a) KFRP fabrication and (b) general dimensions. Nomenclature: extrusion block (1), tape (2), Teflon™ (3), fibre (4), matrix (5).

the optimum testing conditions, both of which are time-consuming and demanding on resources [1,8,13–15]. Numerical methods are essential in streamlining the process and gaining insight into the heat flow phenomena in the inspected part, thus reducing the effort required. Therefore, several commercial codes have been successfully used in the numerical simulation of thermography, such as ABAQUS [16–18], Ansys® [8,12,15,19], COMSOL Multiphysics® [10,20–30] , MSC-Marc® [31], NEi Nastran [32–34], Thermo-Calc® [35] and ThermoHeat-3D Pro [36].

In this work, experimental methods and numerical models developed through Ansys Parametric Design Language (APDL), were used to evaluate the detectability of defects in composite plates produced by Fused-Deposition Modelling. To do so, two sets of inspections were conducted: firstly, using a conventional ATT technique; and secondly, using the DATT technique.

The goal of the first series of experiments was to analyse the differences in the thermal response between specimens with and without fibre reinforcement. This inspection is simulated using the finite element method to gain insight and an in-depth understanding of how the inclusion of the fibres shifts the heat transfer along the thickness of the specimen. The second set of experiments was performed to verify the potential improvement in inspection output as stated in [11]. Therefore, a new finite element method (FEM) model was developed in ANSYS to solve the heat transient problem, which involves the use the surface flux for both heat sources (heating and cooling). Since the essential measurement in thermographic inspection is whether certain types of defects, here voids and delaminations, can be detected, and analytical solutions for the complex heat transfer mechanisms do not exist, the validated FEM model proves to be a valuable tool for the selecting the appropriate inspection parameters. In this case, numerical models were developed and validated for use as a tool to optimize inspection parameters for the DATT in the future.

2. Materials and methods

2.1. Materials

The manufactured composite matrix is made of a biodegradable/biocompatible thermoplastic filament, polylactic acid (PLA), from a filament with 1.75 mm diameter. Three different types of Markforged® continuous fibres (Carbon Fibre (CF), Glass Fibre (GF) and Kevlar® Fibre (KF)) were used for a quantitative comparison of the results [37]. All continuous fibres have a cross-section of 0.4 × 0.35 mm measured on a digital microscope. Each specimen is composed of four layers of fibre, with a fibre bundle of approximately 1000 units.

2.2. Printing conditions

It was observed that the printing conditions presented in Table 1 directly dictate the final quality of the manufactured composite as well as the fibre/matrix interface. Due to differences in mechanical properties of the several fibres used, the printing of each specimen was done by adjusting the printing parameters.

During printing, as depicted in Fig. 1 (a) for Kevlar Fibre Reinforced Polymer (KFRP) specimen, the fibres were aligned with the length of the specimen and the printing direction. A strip of Teflon™ was used to artificially create a delamination defect. The strip was removed after the specimen had cooled down. It was necessary to use tape to secure the Teflon™ until the instant it was overlaid by the nozzle as the airflow from the cooling fan of the extrusion block caused it to blow around. The brass nozzle has a tip and a 45° drilled hole with a 1 mm diameter which allows the simultaneous extrusion of the filament with the fibre.

The final specimens were 120 × 120 × 0.55 mm with two defects of 12 × 50 × 0.5 mm which were longitudinally centred, transversally on the top and at the base as can be seen in Fig. 1 (b). Defect Type I mid-thickness plane was 1.38 mm far from the heated surface. Defects Type II and III were at a distance from the heated surface of 2.75 mm and 4.12 mm respectively. For inspection purposes, the specimen was turned around converting Type I defect into Type III.

2.3. Experimental procedure

To ensure uniform conditions for the experiments, they were performed in a controlled environment, without artificial light, air flows, or movement of people around the station. The only source of light was indirect natural light. The room temperature was monitored to ensure

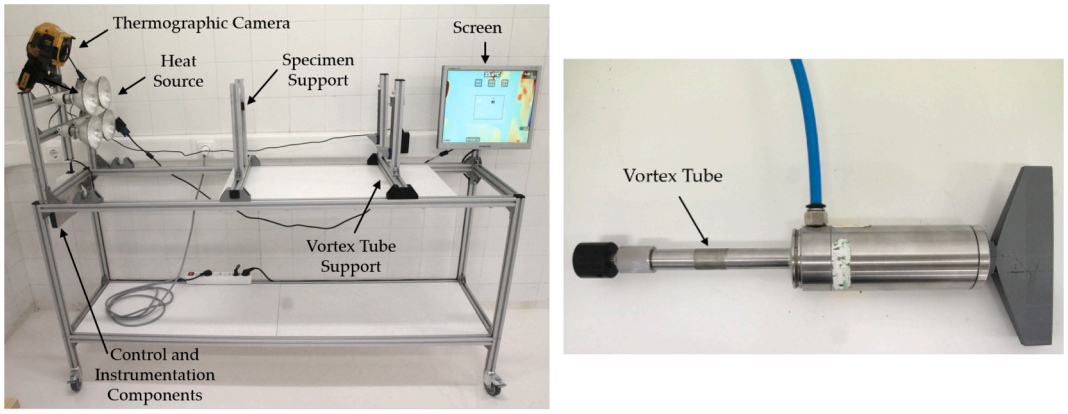

(a) (b)

Fig. 2. Representation of: (a) test station for ATT and DATT and (b) vortex tube used.

Table 2
Technical specifications of the IR camera Fluke Ti400.

Temperature measurement range	−20 to 1200 °C
Noise Equivalent Temperature Difference (NETD)	≤ 0.05 °C (50 mK)
Spectrum	7.5–14 μm
Spatial resolution (iFOV)	2.62 mRad
iFOV on the object	196 μm/pixel

that there was no more than a 2 °C differential between the lowest and highest temperature.

For ATT, the test station depicted in Fig. 2a) consisted of a thermographic camera, a specimen holder, and four Philips PAR38 infrared lamps (total power of 700 W) used as heat source (HS). The set of lamps was perpendicular to the surface of the specimen, providing uniform heating. The specimens were placed at 50 cm from the HS and cooled with natural convection.

A vortex tube is a mechanical device, developed with no moving or electrical parts. It uses compressed air to provide two streams of air: one cold and one hot. The temperatures of both parts are adjusted by a control valve, a generator (fixed part inside the vortex tube) and the pressure of the compressed air supplied. For DATT, the cooling source is provided by the compressed air from the Meech A20400 vortex tube shown in Fig. 2b) placed in its support of the test station formerly set for the ATT.

Both heating and cooling of the test specimen were performed for 20 s. The temperature was monitored for 150 s with the thermographic camera Fluke Ti400, for which technical specifications are listed in Table 2. The test specimen was put aside for 40 min between tests to allow for its return to room temperature. The adjustment of the test time and the instant of switching on the lamps was programmed in LabVIEW® 19.0 commercial software and a DAQmx data acquisition system that interfaces with the computer, both from National Instruments™. For each numerical data, 6 valid tests were considered, and served as a reference for the validation of the numerical models.

3. Numerical model

This section presents the development of the FEM models using the commercial code Ansys® through Ansys Parametric Design Language (APDL). These models were developed to simulate the experimental ATT and DATT inspection procedures. The mesh and geometry, described in section 3.1, were the same for the simulation of both techniques; they differed only in terms of the applied thermal loading conditions, reported in section 3.2.

3.1. Finite element model description

Thermal resistance in composite materials is fundamentally related

Table 3
Fibres, matrix, and air material properties considered in the analysis.

Property	Carbon Fibre	Glass Fibre	PLA	Kevlar® Fibre	Air
ρ [kg·m^{-3}]	1400	1500	1200	1240	1.2
k [W·m^{-1}·K^{-1}]	50	1.3	0.04	0.13	0.03
C_p [J·kg^{-1}·K^{-1}]	400	810	1420	1800	1012

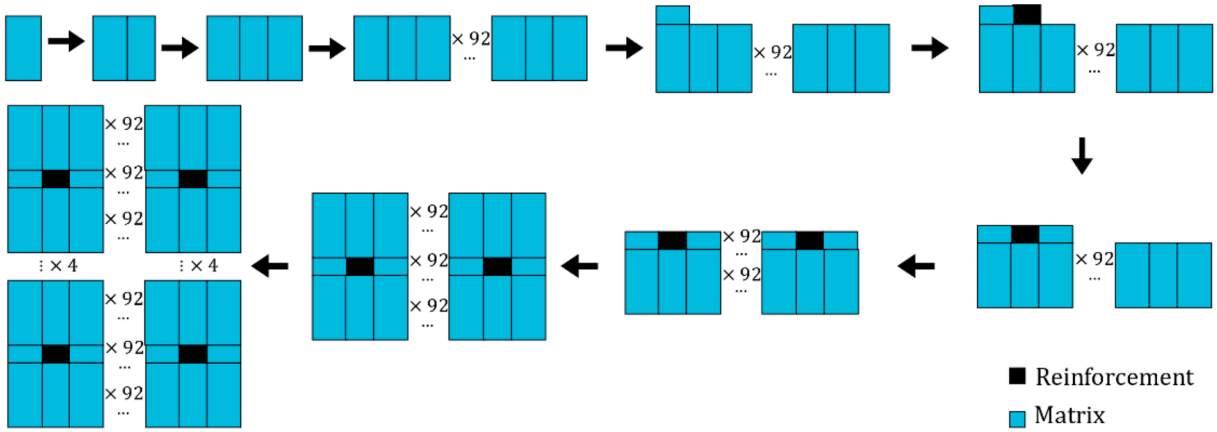

Fig. 3. Schematic representation of the order in which the numerical model was generated.

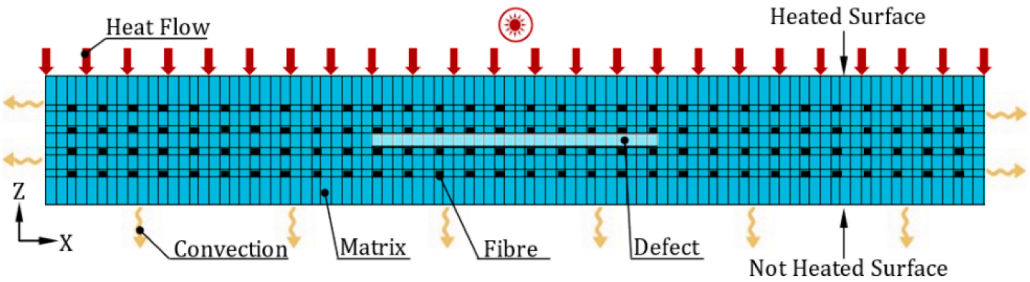

Fig. 4. Simplified representation (not to scale) of the mesh and thermal loads applied to the surfaces.

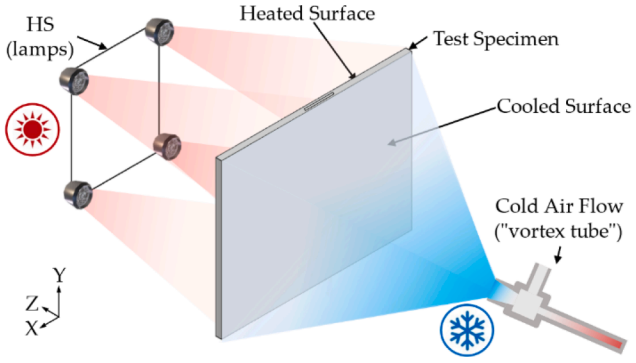

Fig. 5. Schematic representation of DATT.

to two factors: the thermal resistance of the constituent materials and the thermal resistance at the interfaces of these same materials [38]. In the presence of discontinuities such as a delamination, the resistance to heat flow caused by this third feature should also be considered. Therefore, considering that it is possible to disregard the effect of thermal conduction along specimen length, a 2D numerical model was chosen meshed with quadrilateral 2D element PLANE77 with 8 nodes, each with one DOF, namely, the temperature. The geometry of the numerical model was created to match the dimensions of the test specimens, including the fibre and defect dimensions and locations.

In order to generate a uniform mesh of quadrilateral elements, the modelled section of the specimen had to be divided into rectangular areas. The systematic generation of those areas is depicted in Fig. 3, where the black areas contain the elements with the thermal properties of the reinforcement, and those in blue represent the elements with the matrix material thermal properties. The area representing the defect was filled with air, being the material properties of the air [39], fibres and polymer presented in Table 3. The thermal properties of the fibres were not available from the manufacturer. They are, instead, approximate values assumed from the MatWeb database.

In Fig. 4, it is depicted a simplified representation (not to scale) of the mesh used, as well as the boundary conditions applied for the simulation of the ATT. The following nomenclature was adopted for the main surfaces: the heated surface will be designated 'H' (on the side where the heat flux is imposed) and the unheated surface, 'NH' (on the side opposite to the imposition of the heat flux).

3.2. Load application and solution determination

The HS effect was simulated by applying a uniform heat flux on the specimen's surface that is exposed to radiation. Heat exchange with the environment (gains or losses) is accounted for by applying convection on the model surfaces. A positive heat flux value indicates heat flowing to the element's the simulation of the ATT inspection, a uniform heat flux (1550 Wm^{-2}) was applied only on the H surface, and convection (10 $Wm^{-2}K^{-1}$) on the remaining ones; for the simulation of the DATT inspection, a flux of $-2850\ Wm^{-2}$ (cold airflow, therefore the sign must be negative) was applied on the NH surface and 1550 Wm^{-2} on the H surface.

Natural convection was applied on both lateral sides of the specimen. The surface temperature profile, where flows were applied, was recorded for further comparison with the experimental measurements.

As in the experimental tests, two scenarios were considered for the numerical simulation of DATT: "cold and heat applied simultaneously" (CHS) or "first cold and then heat" (CTH). For the CTH scenario, the cold was applied 20 s before the heating started, i.e., as soon as the vortex tube was moved away from the NH surface, the lamps started the heating of the H surface. In Fig. 5 the application modes of heat and cold flow on the specimen surfaces is schematically represented.

The dependence relationship between time and temperature defines this analysis as transient type. All nodes are assigned with a room temperature as a starting point for solving the first iterations and for evaluating temperature-dependent properties if necessary. All simulations had a duration of 150 s.

The temperature from each node or points of interest was acquired with a frequency of 1 s and a time step of 0.1 s. The automatic time-stepping option enables the program to determine the size of the increments between sub-steps and is enabled for two reasons:

1. The ability to estimate the size of the next time step based on the present and previous analysis conditions by making appropriate adjustments.
2. The second feature is related to the bisection component of the time step. Its purpose is to determine whether to reduce the size of the present-time step and repeat this step with a smaller value. The decision is made after successive equilibrium iterations and if adequate convergence is not achieved, the time step is halved and the analysis restarts at the instant when the problem was detected.

The validation of this numerical model will allow a better

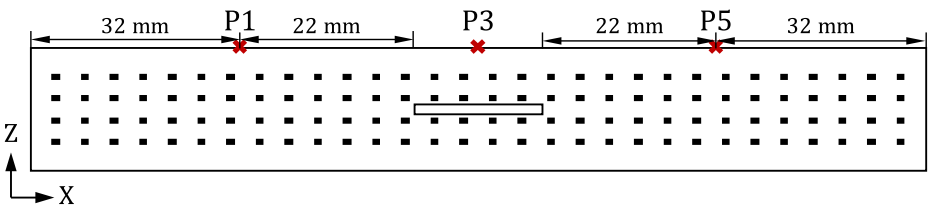

Fig. 6. Schematic representation of the location of the points for temperature data acquisition on a specimen with aligned fibres.

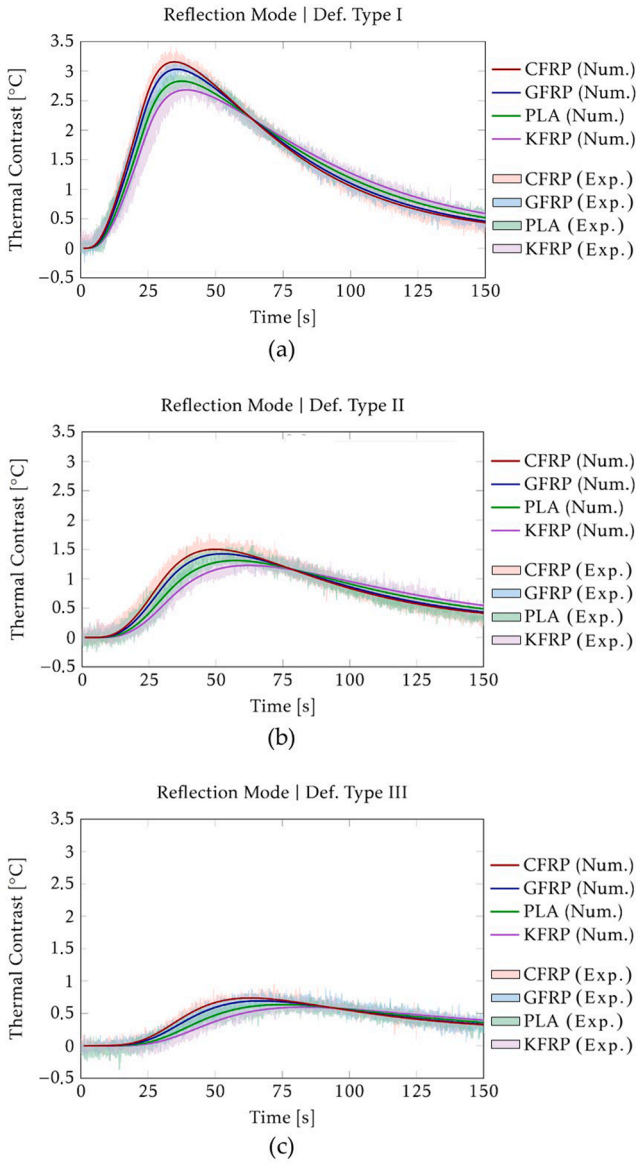

Fig. 7. Variation of numerical and experimental thermal contrast in the specimen with CF for different types of defects and inspection modes for: (a) Defect Type I; (b) Defect Type II and; (c) Defect Type III.

understanding of the working principles of the DATT technique, still little explored in literature, as well as an extended study of different inspection conditions.

4. Results and discussion

The temperature data acquisition was performed at specific regions depicted with points (P), odd numbered, located on the face exposed to radiation of the flat specimen, as shown in Fig. 6.

Although the total lateral dimension of the square specimen is 120 mm, only 100 mm was considered to obtain the temperatures due to the physical drag of the fibres at the end, as seen in Fig. 1. Thus, P1, and P5 are located 22 mm (along the X-axis) from the nearest end of the defect and 32 mm from the nearest edge of the specimen. Point P3 is located at the centre of the surface above and below the defect area. The location of these points is due to the homogenization of the temperature in the regions where they are inserted.

The validation of this numerical model will allow a better understanding of the working principles of the DATT technique, still little explored in literature, as well as an extended study of different inspection conditions. In the context of thermography inspection, defects are detected based on the contrast they present. Mathematically, this is achieved by calculating the difference in temperature between point P3 and the average measured at points P1 and P5, as shown in Fig. 7 and Fig. 10.

Table 4
Instants and numerical values of the maximum thermal contrast for Type I, II and III defects, for different fibre types in ATT.

Defect	CFRP	GFRP	PLA	KFRP
Type I	35 s	36 s	37 s	39 s
	3.16 °C	3.02 °C	2.83 °C	2.68 °C
Type II	50 s	52 s	57 s	62 s
	1.50 °C	1.40 °C	1.31 °C	1.23 °C
Type III	63 s	67 s	75 s	85 s
	0.74 °C	0.70 °C	0.63 °C	0.60 °C

4.1. Active transient thermography

One of the early concerns was related to the use of different types of fibres and how each one would affect the results. In Table 4 are presented the most relevant results for Type I, II and III defects. The earliest instant of maximum contrast was recorded for the Carbon Fibre Reinforced Polymer (CFRP) at 35 s of the test with a value of 3.16 °C. The KFRP, by contrast, was recorded at the later instant 39 s with a maximum contrast of 2.68 °C.

For all the parameters that were analysed, a decreasing thermal contrast for the three defect types was visible in the following order: CFRP, Glass Fibre Reinforced Polymer (GFRP), PLA and KFRP, as shown in Fig. 7. In the same order, the time needed to reach the maximum contrast increased. This was due to the fact that fibres excluding Kevlar have higher thermal conductivity when compared to PLA [40], with effect on the overall thermal conductivity of the composite [41]. Furthermore, the numerical results have a good agreement with the experimental results shown in Fig. 7.

There was a decrease in the maximum peak and a delay in the instant of that value as the defect moves away from the H surface. In the case of the CFRP, from the Type I to the Type II defect there was a reduction of the maximum contrast by 52.5% (1.66 °C) and a delay of 15 s. For the Type III defect, the thermal contrast was 0.74 °C (half of the Type II defect) at 63 s. For the remaining specimens, the same observations were verified with very similar variations in the maximum contrast. The temperature mapping performed by the thermographic camera corresponded to the heat flow reflected at the interfaces of the internal heterogeneities. For this reason, a defect closer to the H surface would be detected earlier since the heat had travelled (emission and return) over a shorter distance relative to any deeper defect. Additionally, there was a lower dissipation of heat in the specimen, and thus a heat accumulation near the H surface causing a higher thermal contrast.

A direct proportionality between the instant of maximum thermal contrast and the square of the defect depth, in reflection mode is known to exist [30,42]. The coefficient of determination, R2 [-], was 0.982 and 0.984 for the numerical and experimental analysis in the case of CFRP specimens' inspection, respectively, which confirmed the good correlation between the two variables in this linear relation, although the inspected parts are very thin, being the depth of the defect quantification unnecessary. In Fig. 7 it is still possible to verify the greater dispersion of the experimental results as the defect depth increased, evidencing the increased difficulty in detecting them as they move away from the H surface. This is mainly due to the attenuation and absorption of thermal energy [28].

The representation of the temperature profile of the specimen NH surface allows the clear localization of the defect along the length of the specimen for both numerical models and experimental tests, due to the localized temperature variation in the defect region. The width

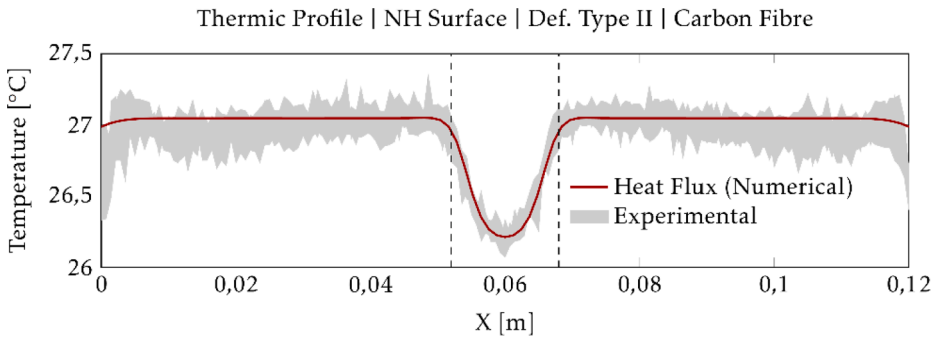

Fig. 8. Numerical and experimental temperature variation along the NH surface of CFRP for the Type II defect at the instant of 51 s.

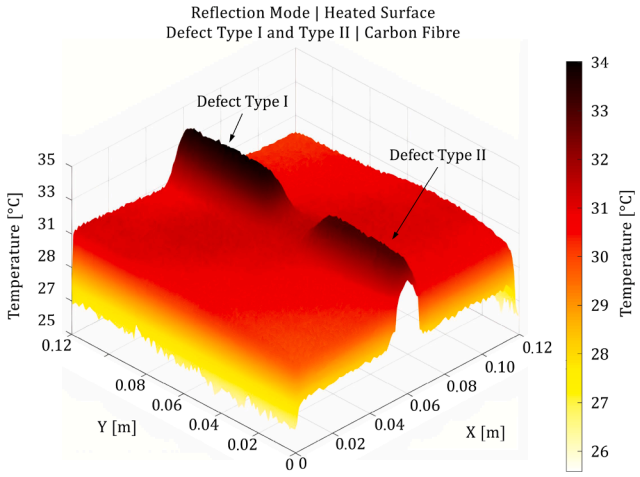

Fig. 9. Graphical representation of the temperatures on the H surface of the CFRP in an experimental test at 50 s.

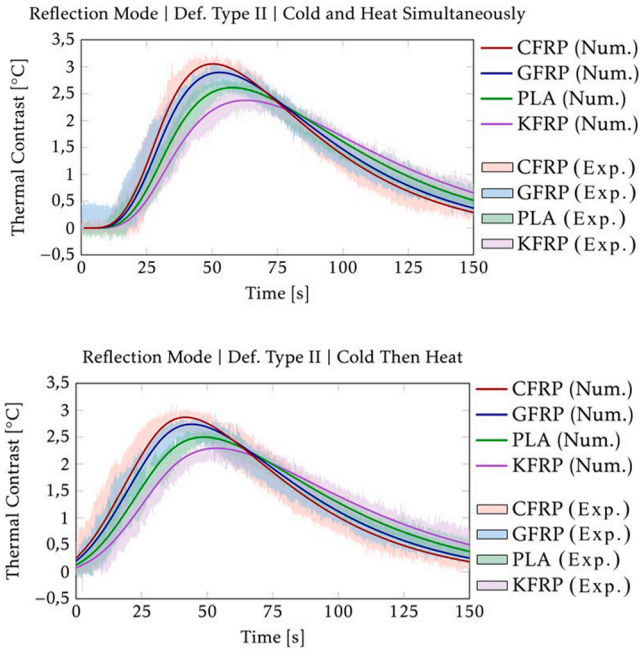

Fig. 10. Variation of numerical and experimental DATT thermal contrast for the Type II defect, different fibre types and in reflection mode.

Table 5
Statistical measurements on the experimental tests in reflection mode of CFRP, in TTA, for the different defects.

Defect	Root Mean Square Error [°C]	Mean Absolute Error [°C]
Type I	0.49	0.43
Type II	0.53	0.47
Type III	0.27	0.24

recognition is therefore another possible output of the thermography inspection or simulation. This recognition, at the time of maximum contrast, in the simulation of ATT inspection of a CFRP specimen with a type II defect is depicted in Fig. 8.

Fig. 9 shows the 3D view of the temperature on the H surface of the CFRP at 50 s during an experimental test. The temperature decay at the edges of the specimen and the symmetrical approach relative to the middle of the length of the specimen can be observed. The two defects that are present (Type I and Type II) can be identified due to the greater topography in these areas.

A variance analysis was conducted considering two standard statistical measures: the Root Mean Square Error (RMSE) and the Mean Absolute Error (MAE) for the CFRP in reflection mode. Both are measures of the accuracy of the results. The first statistical measure is defined as the square root of the mean of the squared errors. This value is never negative and a value of 0 indicates a perfect fit (no errors) between the numerical and experimental data. Due to the square proportion present in the RMSE, it is very sensitive to outliers, that is, the presence of high deviations in the data, even if infrequent, has a disproportionately high effect on the error. A high deviation will have the same effect, or more, than several smaller deviations.

The MAE is the arithmetic mean of the absolute errors present in the sample and contrary to the previous measure is less sensitive to outliers giving equal importance to high or low deviations. It is frequent in time-dependent analyses, as the current one, it is always positive, and a small value indicates a good correlation. It is a very robust metric [43]. Table 5 summarizes the results of the statistical analysis performed for the different defects of the CFRP in reflection mode.

The RMSE tends to be slightly higher than the MAE in the different results due to the greater weight it gives to high deviations. Both statistical measures have confirmed the high accuracy of the results. In these experimental tests, the Type III defect showed the best results, followed by the Type I defect and then the Type II defect.

4.2. *Double active transient thermography*

After analysing the responses of the produced specimens during ATT, the same specimens were inspected using a hot and a cold source, applied on opposite surfaces at different times, as proposed by [11]. This set of simulations and experiments aimed to evaluate the inspection improvements, for composite materials, in terms of temperature contrast and respective time to maximum contrast. Fig. 10 shows the thermal

Table 6
Instants and numerical values of the maximum thermal contrast for Type II defect and different fibre types.

Defect Type II	CFRP	GFRP	PLA	KFRP
Cold Then Heat	42 s	44 s	49 s	54 s
	2.90 °C	2.70 °C	2.50 °C	2.30 °C
Simultaneously	50 s	53 s	58 s	63 s
	3.00 °C	2.80 °C	2.60 °C	2.40 °C
ATT	50 s	52 s	57 s	62 s
	1.50 °C	1.40 °C	1.31 °C	1.23 °C

contrasts for specimens with different fibres in the reflection mode in Type II defect. It is immediately observed that the order in which the results appear is the same, but the time instants are different, and the maximum peaks are significantly higher.

A summary of the numerical results for type II defects of DATT inspection are presented in Table 6, where they can be compared with the results for the ATT simulation.

Firstly, CTH and CHS present, respectively, increases in the maximum contrast between 87% and 100% when compared to conventional ATT. Regarding time, the instants when the maximum contrasts occur where anticipated by 8 s when cold was applied before the heat. When thermic excitations were applied simultaneously, the peak occurred roughly 1 s later.

Secondly, the difference between CTH and CHS is 0.1 °C and 8 s for the most cases, i.e., analysing the trade-off between the two options there is a greater advantage in using CTH since the disproportion in the maximum thermal contrast is much smaller than in the time instants.

5. Conclusions

In this work, two NDT thermographic inspection techniques were analysed and compared: ATT and DATT.

For DATT, the thermal contrast results were found to be 87% to 100% higher in both CTH and CHS scenarios compared with the ATT in Type II defect. It was also observed that the order in which the contrasts for the different specimens appear follows a trend like the ATT technique, i.e., higher thermal contrasts maintaining the same testing parameters follow the thermal conductivity of the materials.

For the different specimens, the order in which the thermal contrasts appear starts with the CTH, then ATT and CHS. In terms of thermal contrast intensity, the order was as follows: CHS, CTH and lastly ATT. Since the ability to detect the effect earlier prevails to the detriment of its maximum value, CTH is the choice for delamination inspection when the operation conditions are granted. The proposed numerical model is validated and ready to be used as a tool for future identification of the best inspection parameters through optimization methodologies.

All numerical results of the ATT and DATT techniques accorded with the experimental results measured. The presence of fibres and their numerical modelling promoted understanding of the thermal phenomena involved and the way the heat dissipated along the thickness, particularly around the fibres. The presence of fibres with thermal conductivity different from the polymer matrix contribute to the change of the heat flux in the specimen affecting the thermal contrast.

Concerning the fibres, the larger its cross section or the number of layers present in the PMC, in the presence of delamination, the greater the thermal contrast and the sooner this will occur. Specimens with CF and GF produce higher thermal contrasts, due to its higher thermal conductivity compared to the polymeric matrix, than KF which thermal conductivity is lower than that of the polymer.

The proposed FEM model can now be used to simulate the ATT and/or DATT inspection of various arrangements of fibre-reinforced polymeric plates obtained by 3D printing. By identifying the optimal inspection parameters, this model can improve the inspection tools and prove useful in the inspection process.

Author contributions

All authors have read and agreed to the published version of the manuscript.

Conflicts of Interest

The authors declare no conflict of interest. The funders had no role in the design of the study; in the collection, analyses, or interpretation of data; in the writing of the manuscript; or in the decision to publish the results.

CRediT authorship contribution statement

Henrique V. Silva: Conceptualization, Methodology, Software, Validation, Formal analysis, Investigation, Resources, Data curation, Writing – original draft, Writing – review & editing, Visualization. **Ana P. Martins:** Software, Validation, Writing – review & editing. **Miguel A. Machado:** Conceptualization, Methodology, Formal analysis, Investigation, Data curation, Writing – review & editing, Supervision, Funding acquisition. **Telmo G. Santos:** Formal analysis, Writing – review & editing, Project administration, Funding acquisition. **Marta S. Carvalho:** Conceptualization, Methodology, Software, Validation, Formal analysis, Investigation, Data curation, Writing – review & editing, Supervision, Funding acquisition.

Declaration of Competing Interest

The authors declare that they have no known competing financial interests or personal relationships that could have appeared to influence the work reported in this paper.

Data availability

Data will be made available on request.

Acknowledgements

Authors acknowledge Fundação para a Ciência e a Tecnologia (FCT - MCTES) for its financial support via the project UIDB/00667/2020 and UIDP/00667/2020 (UNIDEMI).

References

[1] C. Hellier, "Thermal Infrared Testing," in *Handbook of Nondestructive Evaluation*, 1st ed., vol. 1, McGraw-Hill, Ed. McGraw-Hill Education, 2018, pp. 487–533.
[2] T. Santos et al., Reliability and NDT Methods, in Additive Manufacturing Hybrid Processes for Composites Systems. Advanced Structured Materials, vol. 129, Springer, 2020, pp. 265–295.
[3] C. Filippini, D. Cardone, D. Perpetuini, A.M. Chiarelli, L.A. Petitto, A. Merla, Assessment of autonomic response in 6–12-month-old babies during the interaction with robot and avatar by means of thermal infrared imaging, Quant. Infrared Thermogr. J. 20 (2) (Mar. 2023) 78–91, https://doi.org/10.1080/17686733.2021.2025019.
[4] D. Yixian, H. Dexin, D. Zewen, Y. Shuliang, Non-destructive Evaluation Method for Thermal Parameters of Prismatic Li-ion Cell Using Infrared Thermography, Quant. Infrared Thermogr. J. 20 (1) (Jan. 2023) 14–24, https://doi.org/10.1080/17686733.2021.2010380.
[5] R.T. Kidangan, C.V. Krishnamurthy, K. Balasubramaniam, Detection of dis-bond between honeycomb and composite facesheet of an Inner Fixed Structure bond panel of a jet engine nacelle using infrared thermographic techniques, Quant. Infrared Thermogr. J. 19 (1) (Jan. 2022) 12–26, https://doi.org/10.1080/17686733.2020.1793284.
[6] N. Vinnichenko, A. Pushtaev, Y. Plaksina, A. Uvarov, Infrared thermography applied to the surface pressure measurements in insoluble surfactant monolayers, Quant. Infrared Thermogr. J. 20 (1) (Jan. 2023) 1–13, https://doi.org/10.1080/17686733.2021.1989181.
[7] K. Liu, K.-L. Huang, S. Sfarra, J. Yang, L. Yi, Y. Yuan, Factor analysis thermography for defect detection of panel paintings, Quant. Infrared Thermogr. J. 20 (1) (Jan. 2023) 25–37, https://doi.org/10.1080/17686733.2021.2019658.
[8] M.S. Carvalho, A.P. Martins, T.G. Santos, Simulation and validation of thermography inspection for components produced by additive manufacturing,

Appl. Therm. Eng. 159 (February) (2019), 113872, https://doi.org/10.1016/j.applthermaleng.2019.113872.
[9] L. Lei, G. Ferrarini, A. Bortolin, G. Cadelano, P. Bison, X. Maldague, Thermography is cool: Defect detection using liquid nitrogen as a stimulus, NDT E Int. 102 (2019) 137–143, https://doi.org/10.1016/j.ndteint.2018.11.012.
[10] B. Szymanik, T. Chady, K. Goracy, Numerical modelling and experimental evaluation of the composites using active infrared thermography with forced cooling, Quant. Infrared Thermogr. J. 17 (2) (2020) 107–129, https://doi.org/10.1080/17686733.2019.1625243.
[11] M.A. Machado, M.I. Silva, A.P. Martins, M.S. Carvalho, T.G. Santos, Double active transient thermography, NDT E Int. 125 (Jan. 2022), 102566, https://doi.org/10.1016/j.ndteint.2021.102566.
[12] G.P. Malfense Fierro, F. Flora, M. Boccaccio, M. Meo, Real-time automated composite scanning using forced cooling infrared thermography, Infrared Phys. Technol. 118 (2021) 103860, https://doi.org/10.1016/j.infrared.2021.103860.
[13] K. Antin, M. Machado, T. Santos, P. Vilaça, Evaluation of Different Non-destructive Testing Methods to Detect Imperfections in Unidirectional Carbon Fiber Composite Ropes, J. Nondestruct. Eval. 38 (1) (2019) 1–23, https://doi.org/10.1007/s10921-019-0564-y.
[14] F. Pietrarca, M. Mameli, S. Filippeschi, F. Fantozzi, Recognition of wall materials through active thermography coupled with numerical simulations, Appl. Opt. 55 (25) (2016) 6821, https://doi.org/10.1364/ao.55.006821.
[15] R. Waugh, J. Dulieu, S. Quinn, Modelling and evaluation of pulsed and pulse phase thermography through application of composite and metallic case studies, NDT E Int. 66 (2014) 52–66, https://doi.org/10.1016/j.ndteint.2014.04.002.
[16] M. Bayat, M. Safizadeh, M. Moradi, Numerical and experimental study for assessing stress in carbon epoxy composites using thermography, Infrared Phys. Technol. 98 (2019) 108–113, https://doi.org/10.1016/j.infrared.2019.03.003.
[17] M. Barus, H. Welemane, F. Collombet, M.L. Pastor, A. Cantarel, L. Crouzeix, Y. H. Grunevald, V. Nassiet, Bonded repair issues for composites An investigation approach based on infrared thermography, NDT E Int. 85 (2017) 27–33, https://doi.org/10.1016/j.ndteint.2016.10.003.
[18] K. Ghadermazi, M.A. Khozeimeh, F. Taheri-Behrooz, M.S. Safizadeh, Delamination detection in glass-epoxy composites using step-phase thermography (SPT), Infrared Phys. Technol. 72 (Aug. 2015) 204–209, https://doi.org/10.1016/j.infrared.2015.08.006.
[19] P. Pastuszak, Characterization of Defects in Curved Composite Structures Using Active Infrared Thermography, Procedia Eng. 157 (2016) 325–332, https://doi.org/10.1016/j.proeng.2016.08.373.
[20] J. Peeters, C. Ibarra-Castanedo, F. Khodayar, Y. Mokhtari, S. Sfarra, H. Zhang, X. Maldague, J.J.J. Dirckx, G. Steenackers, Optimised dynamic line scan thermographic detection of CFRP inserts using FE updating and POD analysis, NDT E Int. 93 (2018) 141–149, https://doi.org/10.1016/j.ndteint.2016.10.003.
[21] J. Peeters, C. Ibarra-Castanedo, S. Sfarra, X. Maldague, J.J.J. Dirckx, G. Steenackers, Robust quantitative depth estimation on CFRP samples using active thermography inspection and numerical simulation updating, NDT E Int. 87 (87) (2017) 119–123, https://doi.org/10.1016/j.ndteint.2017.02.003.
[22] L. Junyan, L. Liqiang, W. Yang, Experimental study on active infrared thermography as a NDI tool for carbon-carbon composites, Compos. Part B Eng. 45 (1) (2012) 138–147, https://doi.org/10.1016/j.compositesb.2012.09.006.
[23] H. Fernandes, H. Zhang, A. Figueiredo, C. Ibarra, G. Guimarares, X. Maldague, Carbon fiber composite inspection and defect characterization using active infrared thermography: numerical simulations and experimental results, Appl. Opt. 55 (34) (2016) 46–53, https://doi.org/10.1364/ao.55.000d46.
[24] A. Aktas, M. Gower, R. Shaw, R. Simpson, L. Wright, and S. Gnaniah, "Nondestructive testing of defects in thick composites by means of pulse and lock in thermography techniques.," 2015, [Online]. Available: http://www.iccm-central.org/Proceedings/ICCM20proceedings/papers/paper-P205-3.pdf.
[25] J. Peeters, G. Arroud, B. Ribbens, J.J.J. Dirckx, G. Steenackers, Updating a finite element model to the real experimental setup by thermographic measurements and adaptive regression optimization, Mech. Syst. Signal Process. 64–65 (2015) 428–440, https://doi.org/10.1016/j.ymssp.2015.04.010.
[26] J. Peeters, E. Louarroudi, B. Bogaerts, S. Sels, J. Dirckx, G. Steenackers, Active thermography setup updating for NDE: a comparative study of regression techniques and optimisation routines with high contrast parameter influences for thermal problems, Optim. Eng. 1 (19) (2017) 163–185, https://doi.org/10.1007/S11081-017-9368-Z.
[27] V. Kalyanavalli, P.M. Mithun, D. Sastikumar, Analysis of long-pulse thermography methods for defect depth prediction in transmission mode, Meas. Sci. Technol. 31 (1) (2020), https://doi.org/10.1088/1361-6501/ab3b4d.
[28] M. Kaczmarek, A. Nowakowski, Active IR-Thermal Imaging in Medicine, J. Nondestruct. Eval. 35 (1) (2016) 1–16, https://doi.org/10.1007/S10921-016-0335-Y.
[29] F. Khodayar, F. Lopez, C. Ibarra, X. Maldague, Optimization of the Inspection of Large Composite Materials Using Robotized Line Scan Thermography, J. Nondestruct. Eval. 36 (2) (2017) 32, https://doi.org/10.1007/s10921-017-0412-x.
[30] V. Kalyanavalli, T. Ramadhas, D. Sastikumar, Long pulse thermography investigations of basalt fiber reinforced composite, NDT E Int. 100 (August) (2018) 84–91, https://doi.org/10.1016/j.ndteint.2018.08.007.
[31] F. Mabrouki, M. Genest, G. Shi, A. Fahr, Numerical modeling for thermographic inspection of fiber metal laminates, NDT E Int. 42 (7) (2009) 581–588, https://doi.org/10.1016/j.ndteint.2009.02.010.
[32] M. Krishnapillai, R. Jones, M. Bannister, N. Rajic, NDTE of composite structures: Study of lateral heat diffusion effects on thermal contrast, Quant Infrared Thermogr. (2005).
[33] M. Krishnapillai, R. Jones, I. Marshall, M. Bannister, N. Rajic, NDTE using pulse thermography: Numerical modeling of composite subsurface defects, Compos. Struct. 75 (1–4) (2006) 241–249, https://doi.org/10.1016/j.compstruct.2006.04.079.
[34] M. Krishnapillai, R. Jones, I. Marshall, M. Bannister, N. Rajic, Thermography as a tool for damage assessment, Compos. Struct. 67 (2 SPEC. ISS) (2005) 149–155, https://doi.org/10.1016/j.compstruct.2004.09.015.
[35] A. Restrepo and H. Loaiza, 3D discrete model for thermal contrast enhancement and defects depth estimation in CFRP slabs, Ing. y Compet., vol. 16, no. 2, pp. 143–153, 2014, Accessed: Aug. 20, 2021. [Online]. Available: https://www.semanticscholar.org/paper/3D-discrete-model-for-thermal-contrast-enhancement-Girón-Correa/c310912cb07c051d9c7616f6f57f566ce1dbf2ac.
[36] V. Vavilov, D. Burleigh, A. Klimov, Advanced Modeling of Thermal NDT Problems: From Buried Landmines to Defects in Composites, Thermosense XXIV 4710 (2002) 507–521, https://doi.org/10.1117/12.459600.
[37] H.V. Silva, N.P. Catapirra, M.S. Carvalho, T.G. Santos, M.A. Machado, Nondestructive Testing of 3D Printed Fiber-Reinforced Polymeric Composites: An Experimental Critical Comparison, 3D Print Addit. Manuf. (Mar. 2023), https://doi.org/10.1089/3dp.2022.0291.
[38] K. Pietrak, T. Wisniewski, A review of models for effective thermal conductivity of composite materials, J. Power Technol. 95 (1) (2015) 14–24.
[39] F.P. Incropera, D.P. DeWitt, T.L. Bergman, A.S. Lavine, Fundamentals of Heat and Mass Transfer, 7th ed., John Wiley & Sons, 2011.
[40] H. Chen, V.V. Ginzburg, J. Yang, Y. Yang, W. Liu, Y. Huang, L. Du, B. Chen, Thermal conductivity of polymer-based composites: Fundamentals and applications, Prog. Polym. Sci. 59 (2016) 41–85, https://doi.org/10.1016/j.progpolymsci.2016.03.001.
[41] Y. Ibrahim, A. Elkholy, J.S. Schofield, G.W. Melenka, R. Kempers, Effective thermal conductivity of 3D-printed continuous fiber polymer composites, Adv. Manuf. Polym. Compos. Sci. 6 (1) (2020) 17–28, https://doi.org/10.1080/20550340.2019.1710023.
[42] J.G. Sun, Analysis of pulsed thermography methods for detect depth prediction, J. Heat Transfer 128 (4) (2006) 329–338, https://doi.org/10.1115/1.2165211.
[43] R. Pal, Validation methodologies, in: Predictive Modeling of Drug Sensitivity, Academic Press, 2017, pp. 83–107.